Rock mass structural data analysis using image processing techniques (Case study: Choghart iron ore mine northern slopes)

M. Mohebbi[*], A.R. Yarahmadi Bafghi, M. Fatehi Marji and J. Gholamnejad

Department of Mining Engineering, Yazd University, Yazd, Iran

Abstract

Presence of joints and fractures in rocks strongly influences the behavior of the rock mass by dividing the media into smaller units. These structures intensify the potential instability besides the development of sliding and rotational movements. The assumption of discontinuum media changes the whole analysis conditions in relation to the continuum analysis. Acquisition of geometrical and structural discontinuity data alongside their mechanical properties is of paramount importance in a rock mass analysis. Orientation, spacing, expansion, and other geometrical characteristics of the rock mass and their relative geometrical position to the studied projects influence the pattern and potential of failure. Therefore, inevitably, the first step involved in the analysis of rock mass is geometric data collection of the discontinuities as a crucial step before analysis. In this study, the traditional data collection methods in structural discontinuities with their disadvantages are reviewed. Then the discontinuity data collection based on digital image analysis is developed and applied in a case study to several walls of the Choghart iron ore mine. The results obtained show that this method has a very good accuracy in assessing the fine structures, and also it collects data in a much shorter time. This study, therefore, suggests that the proposed method can be used as a practical approach.

Keywords: *Joint Mapping, Digital Image Analysis, Choghart Iron Ore Mine.*

1. Introduction

Rock masses usually contain defects and geometrical discontinuities. This has no direct relation to their inherent and primary properties. These defects are generally foldings, foliations, bedding planes, cleavages, schistosity, joints, and faults [1]. Joints and fractures are often observed in all rock environments especially in carbonated or sedimentary rocks. Joints directly affect the failure mechanism and conditions, fluid flow, etc. in rock mass related projects [2]. Therefore, joint mapping is used to evaluate the geological structures and rock mass classification. It is also used for special purposes such as the analytical and numerical modeling of rock mass stability, rock mass deformation, fluid flow, blasting, rock cutting, and support system design [3]. Nowadays, joint mapping is facing some basic problems including difficulties in discontinuity measurements; low speed of mapping and lack of accuracy, especially in the traditional methods; and difficulties in true structure detection and quantification [2]. Furthermore, different sources of human errors, machine errors, and other complexities challenge the joint mapping [4]. Many efforts have been put on solving these difficulties. Rossini has used the numerical methods to detect discontinuities in 2D noise corrupted functions based on the continuous wavelet transform [5]. Lemu and Hadjigeorgiou have presented a digital face mapping methodology to construct the discontinuity trace maps from photographs of rock faces. For this purpose, the edges have been detected by the "Canny" algorithm, and the adjacent points have been connected to each other using dilation filters. Thinning filters are being applied, and finally,

joint sets are being detected by the artificial neural network-based classification [6]. Leu and Chang have investigated discontinuities in tunnel excavation faces using the image processing techniques in both the spatial and frequency domains [7]. Post has applied various edge and line detection algorithms to extract discontinuity characteristics from digital images. He applied heuristics to detect fracture types and related structures, and used geological criteria to specify the discontinuity network [8]. Kemeny has combined the hough transform and edge detection algorithms for joint tracking from digital images, proposing a simple classification using the detected traces angles [9]. Wang et al. have used the image processing techniques along with the support vector machine (SVM) to detect and classify discontinuities. This algorithm takes multiple images as inputs, and then with the help of SVM classifiers, trained by many training vectors, detects the fractures and classifies them. The fractures are tracked based on the multi-level approach algorithm. They were reduced image noise using low-resolution images, so just thick fractures, had a chance to unfold [10]. In another study, Nguyen et al. have analyzed fracture evolution from inclined flaws (cuts) in a soft rock using high resolution digital photographs and Digital Image Correlation (DIC). They have developed an extended DIC method that allows automatic tracing of discontinuities and their quantification in terms of the displacement jumps along their length [11]. According to Assali et al., the manual field survey method deficiencies can be overcome using the dense 3D measurement techniques such as terrestrial laser scanning and optical imaging to obtain a more complete 3D model and structural statement. Hence, they have developed a semi-automatic process that allows 3D models to be combined with the results of field surveys in order to provide more precise analyses of rock discontinuities. They have combined 3D data and 2D digital images as a support for the structural survey [12]. In a recent supplementary study, they have proposed a combined approach using both 3D point clouds (from LiDAR or image matching) and 2D digital images, gathered into the concept of "solid image". This product is a connection between the advantages of classical true color 2D digital images, accessibility and interpretability, and particular strengths of dense 3D point clouds, i.e. geometrical completeness and accuracy [13].

Many other studies have been carried out in similar fields. However, it should be noted that there exists no commercially available thorough and accurate technique to measure all the required structural data in discontinuity mapping considering the limitations of time, cost, risk, etc. The outcome of most of the studies in this field is the non-commercial codes not available to others. The purpose of this work was the accurate and fast mapping of discontinuities in some walls of the Choghart iron ore mine. Also the best applicable technique in this field will be developed in such a way to provide the required data for development of stability analyses.

2. Traditional methods of discontinuity mapping

Usually there is no direct access to underground in primary stages of an engineering project. In general, outcrops are the main sources of engineering and geo-technical characteristics of rock masses in these stages [3]. Therefore, statistical measurement of structural and mechanical data from the outcrops or other faces becoming available through underground excavation phase should be studied. Applying statistical techniques in processing the data acquired from the outcrops provides valuable information that helps in design stages to simulate joints in an area.

The most conventional and applicable discontinuity mapping methods are the scan line and window sampling techniques [14]. In the scan line method (Figure 1 a), a clean and approximately planar rock face is selected that is large relative to the size and spacing of the exposed discontinuities (roughly 10 to 20 times the average spacing). Each scan line tape is scanned, starting from the zero end, until a discontinuity face is intersected, and then the properties of those intersected discontinuities are recorded [3]. Window sampling provides an area-based sample of discontinuities exposed at a given rock face. The window sampling technique is essentially the same as the scan line sampling, except that all the discontinuities visible within a defined area of the rock face are measured, rather than only those that intersect the scan line (Figure 1 b) [15]. The most important parameters of discontinuities including dip, dip direction, extension, infilling materials and percentage of infilling, roughness, and joint compressive strength are measured.
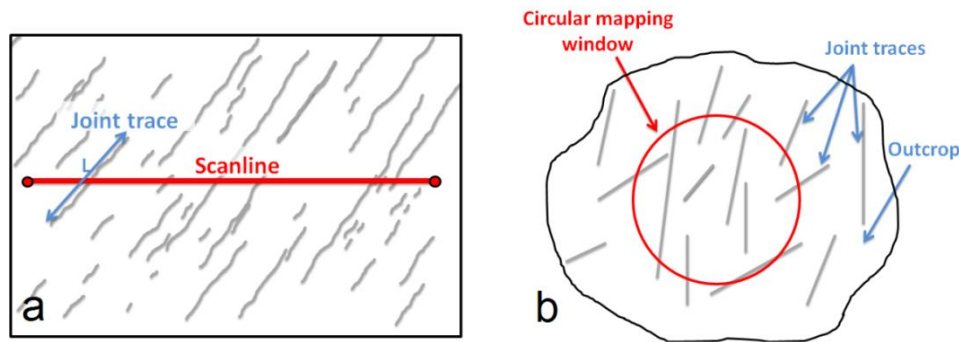
Figure 1. Schematics of measuring structural parameters of discontinuity: a) scan line method b) window sampling [16].

Also an unconventional method of discontinuity mapping is the unparalleled boreholes one. This method obtains the density and characteristics of discontinuities using the least squares method [16]. Furthermore, in geo-physical explorations, the discontinuities' geometry is achieved using properties of longitudinal waves in a tensor called discontinuity tensor [17].

All these methods require certain equipment and conditions that make data collection difficult and time-consuming. Many studies have been focused on fast discontinuity mapping in the recent years.

3. Image discontinuity mapping method

Sampling difficulties, human bias, safety risks, access to rock faces, time and cost limitation, etc. are the most major drawbacks of the traditional discontinuity mapping methods. In order to overcome these shortcomings, the color image processing algorithms have been combined with the discontinuity mapping principles. Applying image processing significantly increases measuring speed and accuracy. The stages involved in developing this method are explained in the following flowchart (Figure 2).
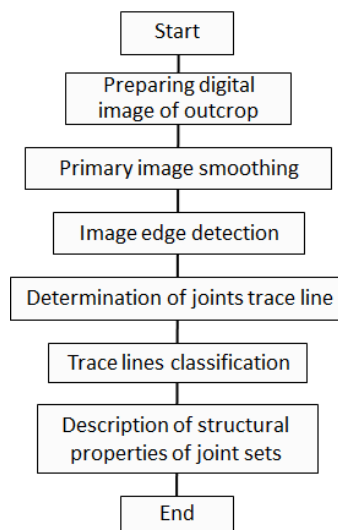

Figure 2. Flowchart of image discontinuity mapping method developed in this study.

3.1. Preparing digital image of outcrop

The first step involved in developing the image-based discontinuity mapping is to acquire high-quality color images from the best outcrops of the desired project. For a maximum efficiency, at least 8 Mpixel resolution and use of CCD (Charged Coupled Device) sensors are being suggested in imaging. Moreover, the camera angle should be perpendicular to the outcrops strike. Due to the need to have a dimension, the outcrops should be marked with an ideal scaling tool. The images with the least color difference and the same lighting must be selected. It should be noted that oblique radiation of light can improve the techniques. Figure 3 is an example of images taken in order to implement this technique on a typical jointed outcrop. The images are turned into gray scale in order to be prepared for the histogram smoothing process (Figure 3).
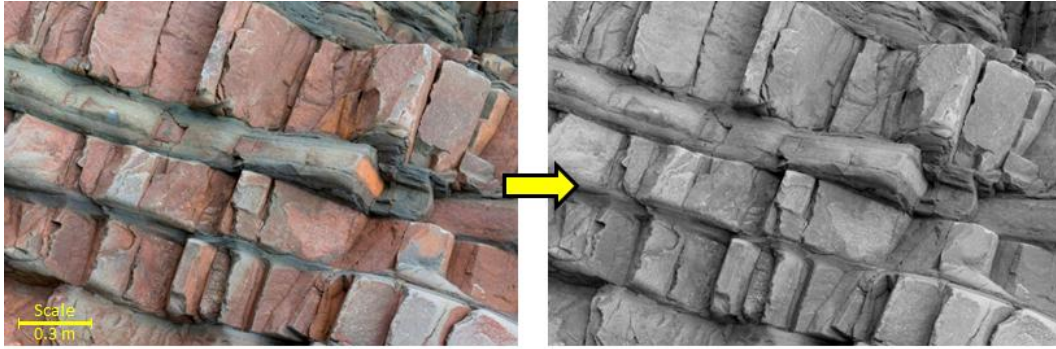
Figure 3. A sample of images taken for discontinuity mapping using image processing.

3.2. Primary image smoothing

Image histogram describes the frequency of the intensity values that occur in an image. The image is preliminary smoothed after converting color image to gray scale. In smoothing, the pixels of an image are modified, intensity of pixels with lower intensity than the adjacent pixels is increased, and some low-frequency intensities are neglected, leading to a smoother image histogram [18]. Three techniques are being used in the smoothing process: histogram stretching, histogram equalization, and local Gama correction [20]. The idea behind histogram stretching is to increase the dynamic range of the gray levels in the image being processed. Thus histogram stretching increases image contrast by specifying the lower and upper limits. Here, values in low-high specify the bottom 1% and top 1% of all the pixel values. Histogram equalization enhances image contrast. This allows for areas of lower local contrast to gain a higher contrast. Suppose a gray scale image {x}, n_i as gray level i occurrence. The probability of existence of a gray pixel i in the image is:

$$p_x(i) = p(x=i) = \frac{n_i}{n}, 0 \le i \le L \tag{1}$$

where L is the number of all gray levels in the image (usually 255), n is the number of all pixels in the image, and $p_x(i)$ is the histogram of color i amount in the image pixel in normalized interval [0,1]. The cumulative distribution function (CDF) of p_x is:

$$cdf_x(i) = \sum_{j=1}^{i} p_x(j) \tag{2}$$

cdf_x is the normalized cumulative histogram of the image. The purpose of the histogram smoothing process is to produce a conversion in the form of $y=T(x)$ to produce a new image {y} by flatted histogram (Figure 4).

The resulting image will have a linear cumulative distribution. Therefore, for some constants K, the following relation may be deduced:

$$cdf_y(i) = iK \tag{3}$$

cdfy is the normalized cumulative histogram of the image. The conversion T maybe calculated using Eq. (4).

$$T = \left(\frac{cdf(i) - cdf_{min}}{cdf_{max} - cdf_{min}} \right) \tag{4}$$

T is a conversion that changes an input image histogram to an output image histogram [19]. Implementation of the stretching and equalization smoother in an image used in this study is shown in Figures 5 and 6.
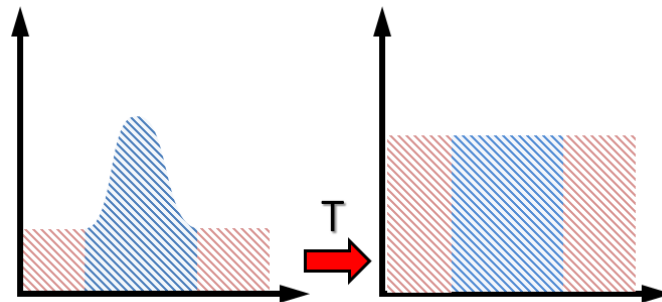

Figure 4. Image histogram in smoothing process of light intensity [19].
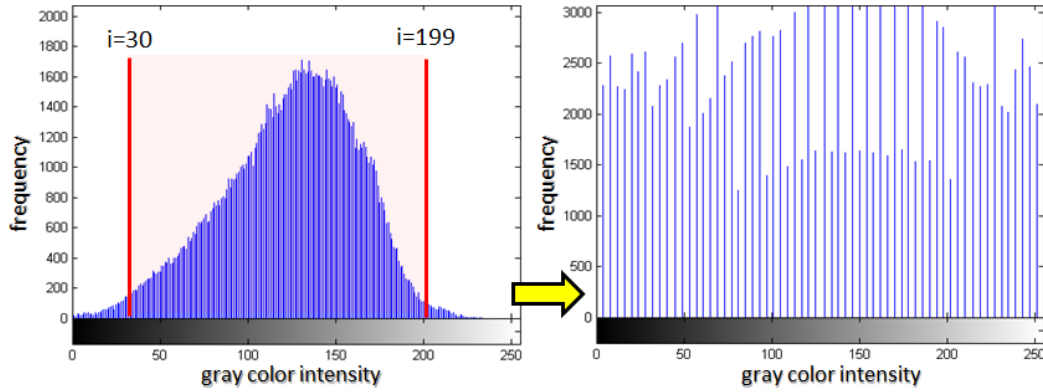
Figure 5. Histogram smoothing process of an outcrop image with low-high stretching limits of 30 and 199, respectively.
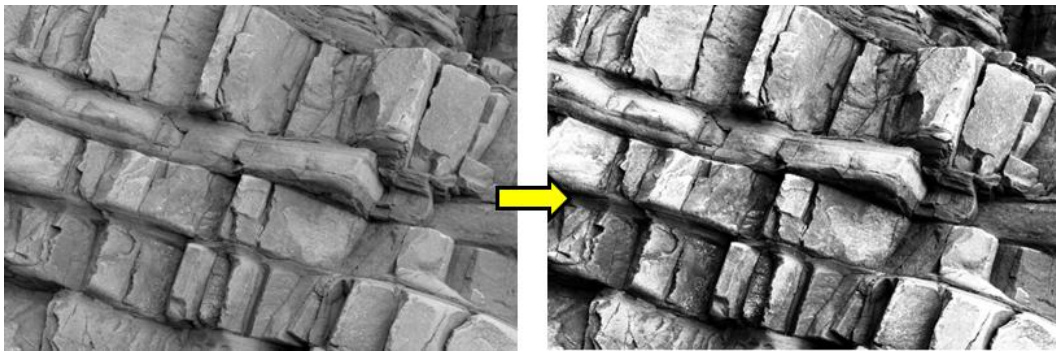

Figure 6. Histogram stretching smoothing results of an outcrop image with low-high stretching limits of 30 and 199, respectively.

Histogram equalization and stretching may not be a suitable objective, where brightness of some areas (or objects) of the image are satisfactory and others are not [20]. Thus the local gamma correction is being applied as the third supplementary smoothing method. In Gamma correction, on each pixel of the image that has a non-linear effect on luminance we have:

$$g(u) = u^{\gamma} \tag{5}$$

In the above equation, u ϵ [0, 1] denotes the image pixel intensity, γ is a positive constant introducing the gamma value, and $g(u)$ is the new pixel intensity after correction. The goal of local gamma correction is to estimate the gamma value of an image in a local approach. The basic idea is the fact that the homogeneity value in an image not suffering from gamma distortion has a lower value (near to zero). These homogeneity values can be calculated by the gray level co-occurrence (GLCM) matrix, measuring the probability that a pixel of a particular gray level occurs at a specified direction and a distance from its neighboring pixels. Here, the homogeneity feature is extracted using GLCM, P, as follows:

$$Hom = \sum_{i=1}^{256} \sum_{j=1}^{256} \frac{P(i,j,d,\theta)}{1+|i-j|} \tag{6}$$

where *Hom* is the homogeneity, *i* is the gray level at the location with coordinate (*x,y*), and *j* is the gray level of its neighboring pixel at a distance *d* and a direction *θ* from a location (*x,y*). The gamma value is then estimated by minimizing these homogeneities in sub-matrices of the image based on [20]. Implementation of the local gamma smoother in an image used in this study is shown in Figure 7. It is clear that the dark areas have become more clear.

Along with smoothing luminance intensity, the image noise must be left out. One of the noise removal purposes is to eliminate the lines that are diagnosed at a later stage due to surface roughness. Here, linear, median, winner, and total variation denoising filters were examined, and the total variation denoising was selected. This is based upon the principle that the signals with excessive and possibly spurious details have high total variation, i.e. the integral of the absolute gradient of the signal is high. According to this

principle, reducing the total variation in the signal subject to it being a close match to the original signal removes the unwanted detail, whilst preserving the important details such as edges. This noise removal technique has advantages over the simple techniques such as linear, median, and winner, which reduces noise but, at the same time, smooths away the edges to a greater or lesser degree. By contrast, the total variation denoising is remarkably effective at simultaneously preserving edges, whilst smoothing away noise in flat regions, even at low signal-to-noise ratios [21]. Consider the 2D signals y such as images. The total variation norm (V) in the isotropic version is:

$$V(y) = \sum_{i,j} \sqrt{\left|y_{i+1} - y_{i,j}\right|^2 + \left|y_{i,j+1} - y_{i,j}\right|^2} \qquad (7)$$

The standard total variation denoising problem is still of the form:

$$\min_y E(x, y) + \lambda V(y) \qquad (8)$$

where E is the 2D L_2 norm, and $\lambda \in (0,1)$ is the regularization parameter. There are many algorithms that solve the variants of this problem. A recent algorithm that solves this is known as the primal dual method, fully discussed in [22]. Figure 8 shows this denoising in the proposed image.
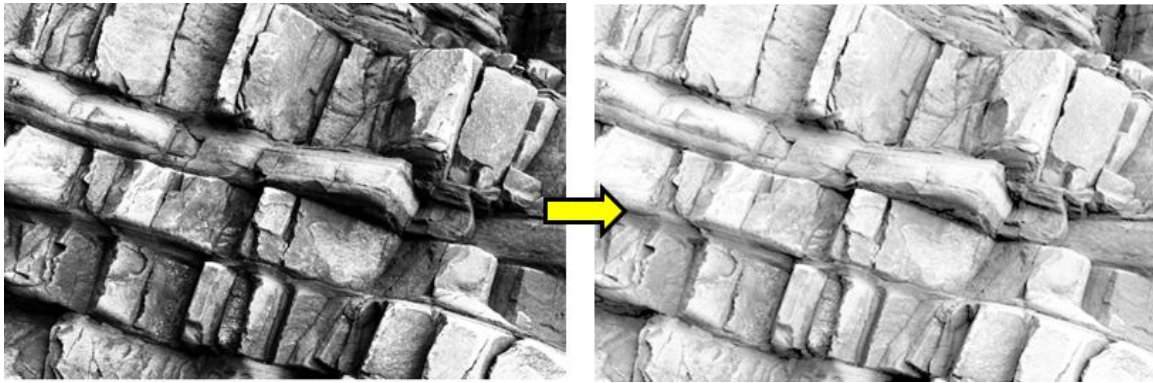

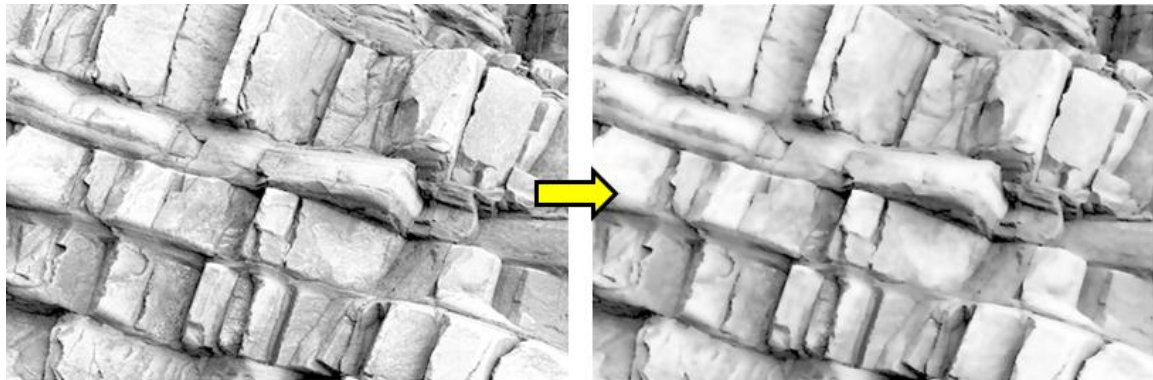**Figure 7. Local gamma smoothing results of an outcrop image.**

Figure 8. Denoising an outcrop image using total variation filter with regularization parameter=0.2 and with selecting Poisson type of noise.

3.3. Image edge detection

Edge detection refers to the process of identifying and locating the sharp discontinuities in an image [23, 24]. Edge detection is the next step after image smoothing. Most edge detection methods may be grouped into the two categories of gradient-based and Laplacian-based edge detection ones. The gradient method detects the edges by looking for the maximum and minimum in the first derivative of the image, while the Laplacian method searches for zero crossings in the second derivative of the image to find edges. Maximum Euclidean distance, Robert's cross operator, Sobel operator, Canny, Prewitt's operator, etc. are of the most important algorithms of edge detection. Based on the results of this study, the Canny edge detection algorithm achieves the best results in image discontinuity mapping.

Canny algorithm basically detects edges with maximum changes of gray intensity. Given a

signal of an edge in the image with the jump intensity shown in the diagram of Figure 9 (a), its derivative (in 1D space with respect to t) creates the diagram in Figure 9 (b). Clearly, the derivative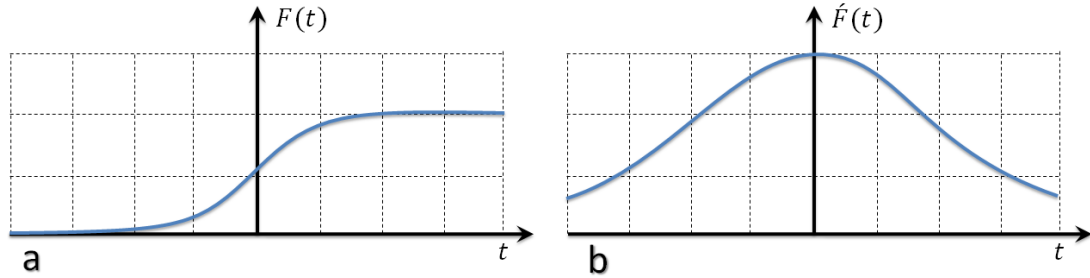 shows a maximum located at the center of the edge in the original signal. Finding these maxima results in the image edge detection. This method of locating an edge is characteristic of the "gradient filter" family of edge detection filters.

Figure 9. Schematic of color variation signal in a) an edge and b) its gradient [25].

Canny algorithm does not directly derivate the image but uses convolution of some operators and images. Sobel operator, as in Eq. (9), in the x and y directions, is used in this study [25].

$$G_x = \begin{bmatrix} -1 & 0 & +1 \\ -2 & 0 & +1 \\ -1 & 0 & +1 \end{bmatrix} G_y = \begin{bmatrix} 1 & 2 & 1 \\ 0 & 0 & 0 \\ -1 & -2 & -1 \end{bmatrix} \quad (9)$$

where G_x and G_y are the applied operators, respectively, in the x-axis and y-axis directions. These operators can then be combined together to find the absolute magnitude and orientation of the gradient at each point using Eq. (10).

$$|G| = \sqrt{G_x^2 + G_y^2} \quad (10)$$

The edge orientation (relative to the pixel grid) is given by Eq. (11).

$$\theta = \tan^{-1}(G_y / G_x) \quad (11)$$

It should be considered that, due to the regular arrangement of pixels, θ can only have the following values: 0° (positive horizontal), 45° (positive diagonal), 90° (negative horizontal), and 135° (negative diagonal). Other values should be modified to these values ($\acute{\theta}$) (Figure 10).
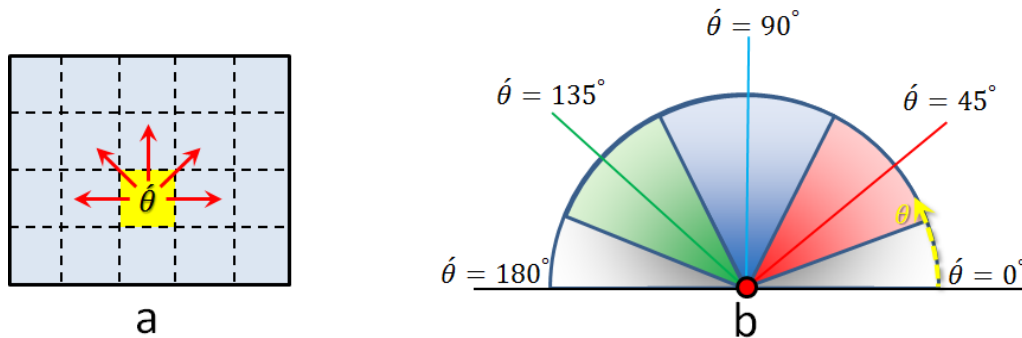

Figure 10. a) Candidate pixels for edge angle calculation b) modification of calculated angles to acceptable values [25].

The gradient of candidate pixels for edge might not be locally maximum. These pixels are compared to their neighbor pixels in gradient direction, and if the gradient of the candidate pixels is lower than at least one of their neighbors, those candidate pixels are removed. Finally, the hysteresis threshold algorithm takes two thresholds, a high T_1 and a low T_2. Any pixel in the image that has a value greater than T_2 is presumed to be an edge pixel, and is marked as such immediately. Then any pixel that is connected to this edge pixel and that has a value greater than T_1 is also selected as an edge pixel. The values $T_1=0.5$ and $T_2=0.2$ are selected in this study. Figure 11 shows the implementation of some of the most important edge-detection algorithms in the image used in this study.

It should be noted that there is no concern about unrealistic boundaries such as rubbles, shadows, and tape line because they are removed during the clustering stage.
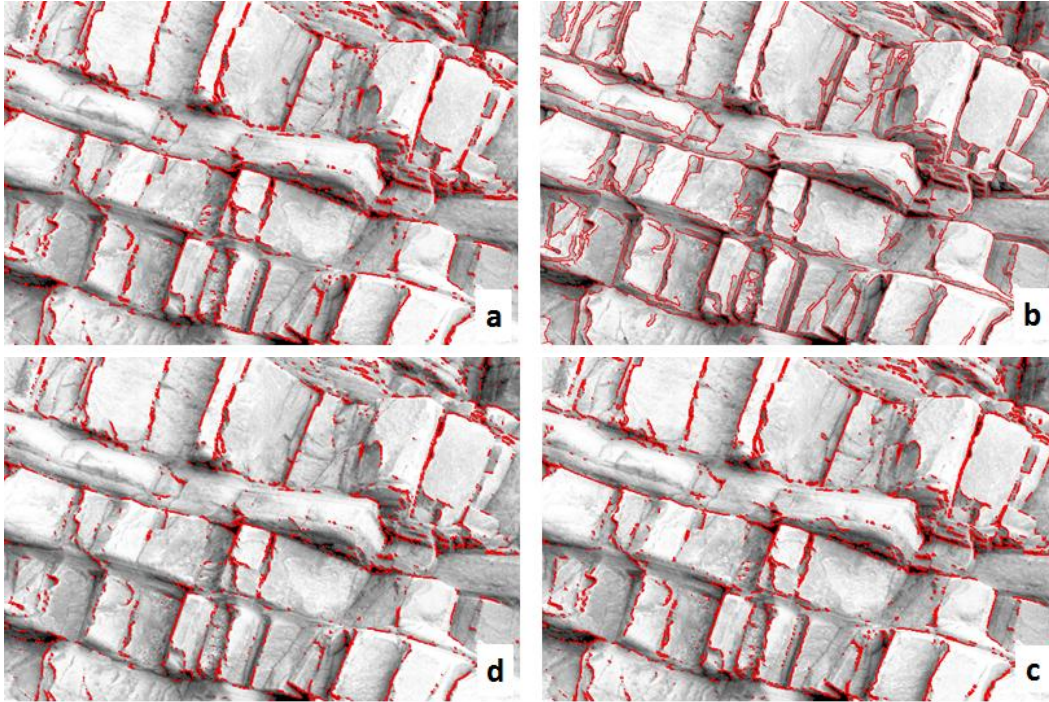
Figure 11. Edge detection of an outcrop image using a) Prewitt's operator, b) Canny operator, c) Robert's operator, and d) Sobel operator.

3.4. Determination of joint trace line

Because of the straight nature of rock joints, edges with straight lines should be separated from those with curvilinear lines. The Hough transform algorithm is used for this purpose [18]. This algorithm can connect the separate lines that are in one direction, resulting in a trace line.

In general, any straight line can be represented as a point in the Hough space. As illustrated in Figure 12 a, a straight line may be presented by the angle of normal to the line (θ) and the distance from the origin of coordinate system (ρ). In image space (x, y), a straight line may be presented by Eq. (12).

$$x \cos \theta + y \sin \theta = \rho \qquad (12)$$

If θ is in $\left[\frac{-\pi}{2}, \frac{\pi}{2}\right]$, the parameters obtained are unique, and each line in the x-y plane corresponds to a point in the θ-ρ plane. Consider a series of

points $\{(x_1, y_1), \ldots, (x_n, y_n)\}$. These points are transformed to sinusoids in plane using Eq. (13).

$$x_i \cos \theta + y_i \sin \theta = \rho \qquad (13)$$

If a series of points in a space lie on a straight line, the corresponding lines in the plane transform intersect in a point. This point location is equal to the parameters θ and ρ of that straight line. Therefore, instead of finding a straight line in image space, the intersection points can be found in the Hough space. Since the lines in an image space are not exactly straight, the curves in the parameter space do not intersect exactly at a single point. Therefore, Hough space is gridded as shown in Figure 12 (b). The measurements are done based on this grid. The accuracy of Hough transform depends on the cell dimensions shown by $\Delta\theta$ and $\Delta\rho$.
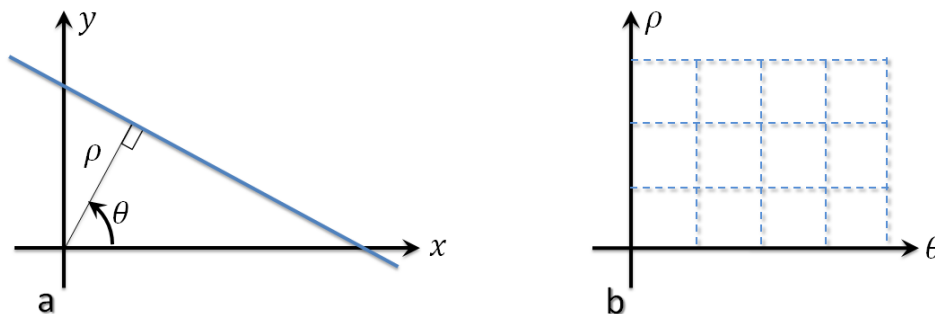

Figure 12. a) A straight line components, b) Gridding in Hough space [18].

All the points detected as edge are mapped to parameter space, and using Eq. (9), each point corresponding curve is obtained in parameter space. The cell value increases by one if a curve passes through it. After applying all curves, the coordinates of the center of the cells with values higher than a threshold are considered as

parameters of a straight line in the space image plane [15]. The trace length characteristic (L) can be calculated using the distance of the determined initial and final points. Figure 13 illustrates the application of this algorithm to the detected edges by the Canny edge detection algorithm.
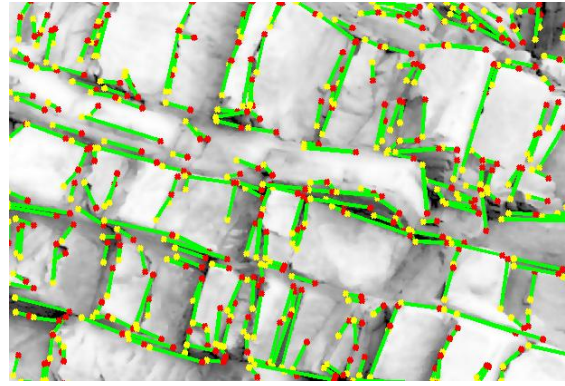
Figure 13. Implementation of Hough transform algorithm in edge detection, and presenting joint trace lines.

3.5. Classification of trace lines

By determination of trace lines, the existing joint sets in the image must be calculated. Determination of clusters is an important step in determining joint sets. Here, the subtractive clustering algorithm is used to determine clusters. It is a fast, one-pass algorithm used for estimating the number of clusters and the cluster centers in a set of data. In this algorithm, all points are considered as centers, and then the density around each point x_i is calculated based on Eq. (14).

$$dxj = \frac{\left(x_i - x_j\right)}{rad_i}, \text{ for } j=1 \text{ to number}(n) \quad (14)$$

$$dens_i = \sum_{j=1}^{n} e^{-4dxj} \quad (15)$$

rad_i is the clustering radius in interval (0,1). The value for *dens* shows the density of points around each point. The point with the highest value is selected as the first joint set center, and this point and all points included in the current set are removed. The procedure is repeated until all points are removed. Following this method, the number of joint sets may be appropriately determined. The convergence radius increased from 0.06 to 0.5 with 0.01 interval steps. The final number of clusters is determined when the number of clusters does not change in three consecutive radii [26].

Fuzzy c-means (FCM) algorithm is used to determine the center and member of each cluster. It is a method of clustering that allows one piece

of data to belong to two or more clusters. The purpose of this algorithm is to assign a fuzzy partitioning to a group of characteristics in c cluster$\{P_1, \dots, P_n\}$ with representatives $\{g_1, \dots, g_c\}$ so that locally minimizes Eq. (16) that measures the relation between the clusters and groups of clusters' representatives.

$$J = \sum_{K=1}^{n} \sum_{i=1}^{c} \left(u_{ik}\right)^m \Phi(x_k, g_i) =$$

$$\sum_{K=1}^{n} \sum_{i=1}^{c} \left(u_{ik}\right)^m \sum_{j=1}^{p} \left(x_k^{\;j} - g_i^{\;j}\right)^2 \quad (16)$$

where u_{ik} is the degree of belonging of each characteristic k in cluster P_i, and $\emptyset(x_k, g_i)$ is the Euclidean distance between a pair of characteristic vectors. The parameter *m*, which is fuzzy partition matrix exponent in $(1,\infty)$ interval, controls the degree of fuzziness of degree of belongings for characteristic K. In this presentation, the degree of belonging of each characteristic to cluster P_i is constant, and g_i of P_i cluster is updated using Eq. (17) to minimize Eq. (16). When assigning the degree of belonging, u_{ik} of each characteristic k in cluster P_i is calculated using Eq. (18).

Figure 14 shows the implementation of this algorithm in one of the images of rock masses in wall of the Choghart iron ore mine.

$$g_i = \frac{\sum_{k=1}^{n} (u_{ik})^m x_k}{\sum_{k=1}^{n} (u_{ik})^m} \qquad (17)$$

$$u_{ik} = \left[\sum_{n=1}^{c} \left\{ \frac{\sum_{j=1}^{p} \left(x_k^{\ j} - g_i^{\ j}\right)^2}{\sum_{j=1}^{p} \left(x_k^{\ j} - g_h^{\ j}\right)^2} \right\}^{\frac{1}{m-1}} \right]^{-1} \qquad i = 1,...,c \qquad (18)$$
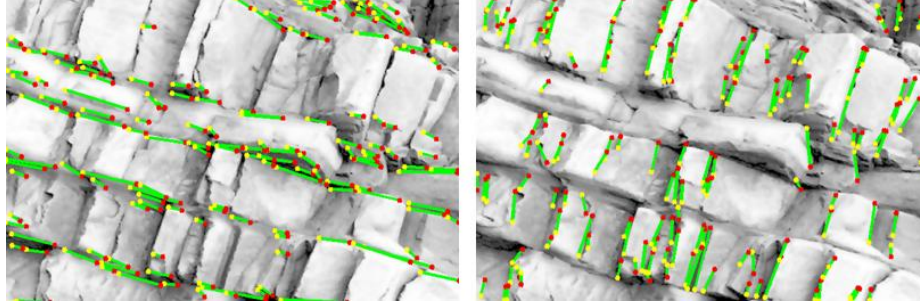

Figure 14. Clustering trace lines in four joint sets using FCM algorithm.

3.6. Description of structural properties of joint sets

Trace lines and classification of joint sets were detected following the presented computation stages. Now some geometrical properties of joint sets may be calculated. The current algorithm can calculate orientation, extension, and spacing for each joint set and linear density and overall rock mass quality index.

The values for parameter ρ are used to calculate spacing. Sorting values in the ascending order, one can use the following relation to calculate the distance of a joint from its neighbor joints.

$$s_r = r_i - r_{i-1}$$
$$s_l = r_{i+1} - r_i \qquad (19)$$

where s_r and s_l are the spacings from the right and left sides, respectively. When there are multiple joint sets, the average spacing for the whole rock mass may be found using Eq. (20).

$$\frac{1}{S_t} = \sum_{i=1}^{n} \frac{1}{S_i} \qquad (20)$$

where S_t is the average spacing for the whole rock mass, n is the number of joint sets, and S_i is the average spacing of each joint set. The average linear density of rock mass may be estimated using Eq. (21).

$$d_{av} = \frac{1}{S_t} \qquad (21)$$

where d_{av} is the linear density of the rock mass and S_t is the average spacing of the rock mass. Rock quality index (*RQD*) may be extracted from the digitized lines produced in the edge detection, by defining a scan line and measuring segments longer than 10 *cm*. The presented technique in this study allows determination of joint extensions as well. A joint may be detected as several joints in one direction. In order to avoid this problem, firstly, the lines in one direction are determined, and then the sum of all line lengths is considered as the joint extension.

The mathematical relations between the 3D properties of fractures (dip, dip direction, and dispersion coefficient) and fractures trace in two dimensions. It is assumed that discontinuity orientations follow Fisher distribution. Therefore, the joint sets are determined by average dip and dip direction and Fisher coefficient based on an approximate initialization from the traditional mapping of some discontinuities. Knowing the orientation of slope in the image, traces of these joint sets in the outcrop are determined based on several geometrical relations. The results are compared to the results of recorded traces in image processing. An objective function (Eq. 22) is used to estimate orientations as an optimization problem with more accuracy. The objective function is an error function between average (μ), standard deviation (σ), and bias (θ) of trace angles of mapped joints and average, standard deviation, and bias of calculated joints.

$$e\left(\mu_T, \sigma_T, \theta_T\right) = A\left(\mu_T - \mu_I\right)^2 + B\left(\sigma_T - \sigma_I\right)^2 + C\left(\theta_T - \theta_I\right)^2 \qquad (22)$$

where index T denotes the calculated data by the program, and index I stands for the fractures trace in the image. The influence coefficients A=0.7, B=0.3, and C=0 were used, and the bias effect

was neglected. The "particle swarm optimization" (PSO) method is used to minimize this function. This is a computational method that optimizes a problem by iteratively trying to improve a candidate solution with regard to a given measure of quality. PSO optimizes a problem by having a population of candidate solutions, here, dubbed particles, and moving these particles around in the search-space according to simple mathematical formulae over the particle position and velocity. Each particle movement is influenced by its local best known position but is also guided toward the best known positions in the search-space, which are updated as better positions found by the other particles. This is expected to move the swarm toward the best solutions.

4. Method verification

The method developed in this study provides a new technique that can successfully increase the speed and accuracy of the structural data collection and analysis of related projects to rock discontinuous environments. It has been tried in the development of this technique to optimize the method, especially in terms of the orientation information. The results of traditional discontinuity mapping and image discontinuity mapping are compared to evaluate the accuracy of the results obtained from this method. Figure 15 shows this comparison for a zone where one of the images was previously processed.

Also Table 1 demonstrates the match error in these discontinuity mapping methods.

In this work, it was tried to calculate the 3D joint parameters based on 2D images. Thus the authors think that these error values can be acceptable, although they suggest that further efforts should be made to increase accuracy.
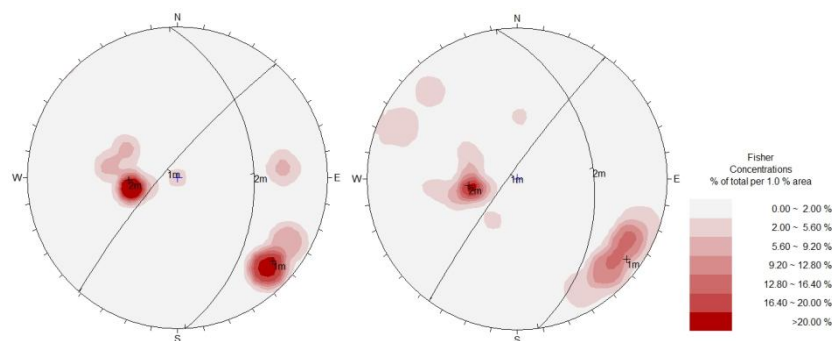

Figure 15. Comparison of joint concentration curves and detected joint sets using a) traditional mapping and b) image processing.

Table 1. Match error of orientation parameters obtained by traditional discontinuity mapping and image processing.

Parameter	Error in matching (%)		
	Joint set 1	Joint set 2	Average
Dip (°)	6.56	5.62	6.09
Dip Direction (°)	5.14	1.54	3.34

5. Method implementation

The central iron ore mine (Choghart) is one of the largest and oldest iron ore open pit mines in Iran. It is located in central Iran. The mine is 132 *Km* SE of Yazd, close to Bafgh. Its pit has walls as long as 500 *m*. The stability of these walls has always been a point of interest in the design and development stages. Figure 16 shows the location of this mine.

The image processing technique is applied to the north walls of this mine to acquire the discontinuitiy properties for further stability analyses. 15 digital images with appropriate quality were taken from 5-m scan lines in different locations. The images were analyzed separately using the image processing techniques mentioned in the earlier sections. Figures 17 and 18 show the statistical analysis of spacing and persistency parameters in the images of one of the zones in the walls, respectively. The complete results obtained from the analyses of these images are demonstrated in Table 2.

In these analyses, *RQD* and linear density were not measured.
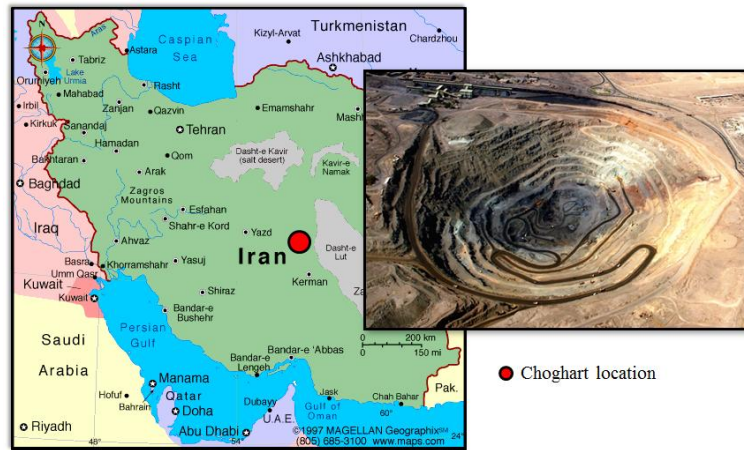
Figure 16. Central iron ore mine (Choghart) location.
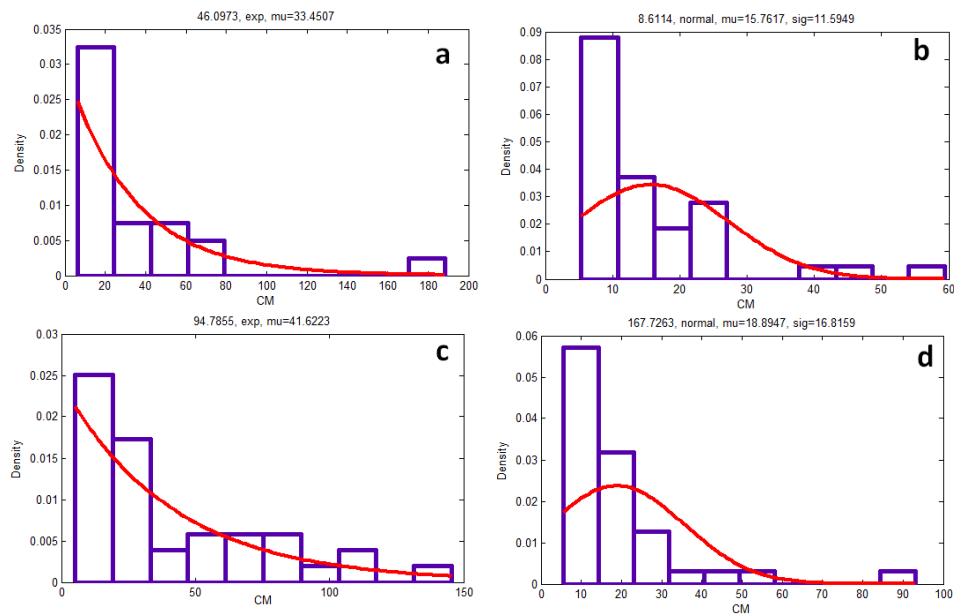

Figure 17. Frequency density and statistical distribution match of spacing in joint sets a) 1, b) 2, c) 3, and d) 4.
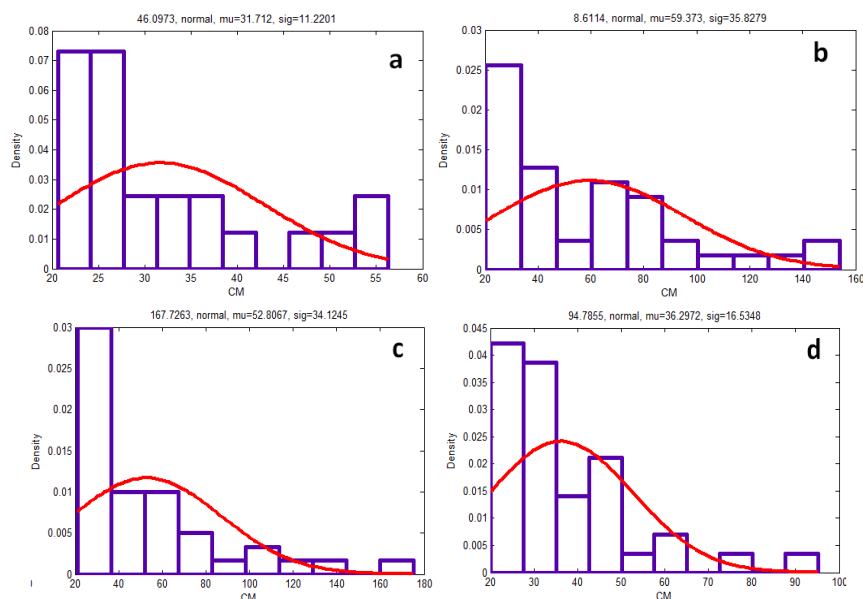

Figure 18. Frequency density and statistical distribution match of persistency in joint sets a) 1, b) 2, c) 3, and d) 4.

Table 2. Results of discontinuity mapping using image processing of scan lines in north wall of Choghart mine.

Image number	Joint set	Spacing (Cm)			Continuity (Cm)			Dip (°)	Dip Direction (°)
		Statistical distribution	Average	Standard deviation	Statistical distribution	Average	Standard deviation		
1	1	Normal	16.16	12.24	Normal	58.2	34.7	45.53	174.16
	2	Normal	25.78	17.16	Normal	28.5	20.4	67.34	203.78
	3	Normal	31.7	*	Log-normal	3.33	0.31	88.12	12.77
	4	Normal	16.55	9.88	Normal	47.46	27.55	77.55	46.46
2	1	Log-normal	2.54	0.53	Log-normal	3.71	0.65	69.64	62.55
	2	Exponential	25.7	*	Log-normal	3.35	0.58	10.58	29.52
3	1	Log-normal	2.48	0.55	Log-normal	3.62	0.68	86.94	243.30
	2	Log-normal	2.43	0.52	Normal	45.08	29.44	35.31	3.06
4	1	Log-normal	2.54	0.66	Log-normal	3.5	0.63	87.82	277.98
	2	Log-normal	2.46	0.47	Normal	39.47	27.12	19.32	5.64
5	1	Log-normal	2.53	0.56	Log-normal	4.08	0.76	89.67	52.73
6	1	Log-normal	2.57	0.74	Normal	43.87	34.61	65.32	234.13
7	1	Log-normal	2.48	0.63	Log-normal	3.52	0.88	27.51	337.05
8	1	Log-normal	2.48	0.61	Log-normal	3.22	0.72	83.99	299.52
	2	Log-normal	2.4	0.65	Exponential	48.18	*	28.41	358.97
9	1	Exponential	27.38	*	Normal	41.48	21.03	79.67	246.71
	2	Exponential	40.24	*	Log-normal	22.2	10.5	15.79	305.74
	3	Exponential	31.52	*	Normal	37.02	15.93	10.83	358.91
	4	Exponential	33.71	*	Normal	36.86	18.67	61.89	223.57
	5	Exponential	15.96	11.76	Log-normal	3.77	0.62	13.3	192.99
10	1	Log-normal	2.56	0.67	Log-normal	3.95	0.56	76.47	253.29
11	1	Exponential	29.29	*	Normal	40.8	22.14	20.88	126.28
	2	Log-normal	2.9	0.73	Normal	36.49	16.8	0	283.93
	3	Exponential	28.33	*	Normal	31.33	11.69	10	104.99
	4	Exponential	25.34	*	Normal	39	22.17	1.87	6.3
12	1	Log-normal	2.83	0.79	Log-normal	3.68	0.49	75.90	262.06
	2	Log-normal	10.52	0.65	Log-normal	30.52	0.85	15.22	193.56
13	1	Log-normal	2.83	0.79	Log-normal	25.65	0.65	18.76	160.36
14	1	Log-normal	2.83	0.79	Log-normal	25.36	0.79	89.81	256.51
15	1	Log-normal	2.83	0.79	Log-normal	25.3	0.78	15.19	19.73

6. Conclusions

The image discontinuity mapping was used to measure the structural discontinuity data of the north wall of the Choghart iron ore mine. The purpose of this work was to improve the accuracy and speed of measurement, while eliminating the human and machine errors. For this, a number of algorithms were developed to estimate the trace line data of joints by processing an input image of the outcrop. This data was utilized to achieve information on a traditional discontinuity mapping using the statistical techniques and some mathematical assumptions.

The image processing technique was able to correctly detect the joint sets of outcrops. It provided a detailed and accurate information on spacing, orientation, extension, etc. The estimated statistical distributions for spacing in most of the outcrops were exponential and log-normal. The statistical distributions of continuity were mostly log-normal and normal. These findings are in agreement with other studies [10]. Comparison of the traditional and image processing results for orientation showed a close agreement. This agreement can be further increased. The measurements in this study can be used to analyze the stability of discontinuous systems in the north walls of the Choghart iron ore mine in further studies. Therefore, due to the selection of discontinuous analysis for this area, and the inability of the rock mass quality classification systems in this type of analysis, the authors did

not consider the qualitative parameters such as RMR, RQD, etc.

References

[1]. Proctor, R.V., White, T.L. and Terzaghi, K. (1977). Rock tunneling with steel supports. Commercial Shearing.

[2]. Bisdom, K. (2011). Modelling 3D Discrete Fracture Networks using 2D outcrop data (Doctoral dissertation, TU Delft, Delft University of Technology).

[3]. Priest, S.D. (1993). Discontinuity analysis for rock engineering. Springer Science & Business Media.

[4]. Kemeny, J. and Post, R. (2003). Estimating three-dimensional rock discontinuity orientation from digital images of fracture traces. Computers & Geosciences. 29 (1): 65-77.

[5]. Rossini, M. (1998). 2D-discontinuity detection from scattered data. Computing. 61(3): 215-234.

[6]. Lemy, F. and Hadjigeorgiou, J. (2003). Discontinuity trace map construction using photographs of rock exposures. International Journal of Rock Mechanics and Mining Sciences. 40 (6): 903-917.

[7]. Leu, S.S. and Chang, S.L. (2005). Digital image processing based approach for tunnel excavation faces. Automation in construction. 14 (6): 750-765.

[8]. Post, R. (2001). Characterizing of joints and fractures in a rock mass using digital image processing (Doctoral dissertation, MS Thesis, University of Arizona).

[9]. Kemeny, J., Mofya, E., Holmlund, J. and Ahlgren, S. (2002). Digital imaging for rock mass characterization. In Geophysics 2002. The 2nd Annual Conference on the Application of Geophysical and NDT Methodologies to Transportation Facilities and Infrastructure.

[10]. Wang, W., Liao, H. and Huang, Y. (2007). Rock fracture tracing based on image processing and SVM. In Natural Computation, 2007. ICNC 2007. Third International Conference on IEEE 1: 632-635.

[11]. Nguyen, T.L., Hall, S.A., Vacher, P. and Viggiani, G. (2011). Fracture mechanisms in soft rock: identification and quantification of evolving displacement discontinuities by extended digital image correlation. Tectonophysics. 503 (1): 117-128.

[12]. Assali, P., Grussenmeyer, P., Villemin, T., Pollet, N. and Viguier, F. (2014). Surveying and modeling of rock discontinuities by terrestrial laser scanning and photogrammetry: Semi-automatic approaches for linear outcrop inspection. Journal of Structural Geology. 66: 102-114.

[13]. Assali, P., Grussenmeyer, P., Villemin, T., Pollet, N. and Viguier, F. (2016). Solid images for geostructural mapping and key block modeling of rock discontinuities. Computers & Geosciences.

[14]. Wei, Z.Q., Egger, P. and Descoeudres, F. (1995). Permeability predictions for jointed rock masses. In International journal of rock mechanics and mining sciences & geomechanics abstracts. Pergamon. 32 (3): pp. 251-261.

[15]. Hoek, E. and Bray, J.D. (1981). Rock slope engineering. CRC Press.

[16]. Karzulovic, A. and Goodman, R.E. (1985). Determination of principal joint frequencies. In International Journal of Rock Mechanics and Mining Sciences & Geomechanics Abstracts. Pergamon. 22 (6): 471-473.

[17]. Oda, M., Yamabe, T. and Kamemura, K. (1986). A crack tensor and its relation to wave velocity anisotropy in jointed rock masses. In International Journal of Rock Mechanics and Mining Sciences & Geomechanics Abstracts. Pergamon. 23 (6): 387-397.

[18]. Gonzalez, R.C. and Woods, R.E. (2002). Digital image processing.

[19]. Hum, Y.C., Lai, K.W. and Mohamad Salim, M.I. (2014). Multiobjectives bihistogram equalization for image contrast enhancement. Complexity. 20 (2): 22-36.

[20]. Amiri, S.A. and Hassanpour, H. (2012). A preprocessing approach for image analysis using gamma correction. International Journal of Computer Applications. 38 (12): 38-46.

[21]. Strong, D. and Chan, T. (2003). Edge-preserving and scale-dependent properties of total variation regularization. Inverse Problems. 19: S165-S187.

[22]. Chambolle, A. (2004). An algorithm for total variation minimization and applications. Journal of Mathematical Imaging and Vision. 20: 89-97.

[23]. Gonzalez, R.C., Woods, R.E. and Eddins, S.L. (2004). Digital image processing using MATLAB. Pearson Education India.

[24]. Maini, R. and Aggarwal, H. (2009). Study and comparison of various image edge detection techniques. International journal of image processing (IJIP). 3 (1): 1-11.

[25]. Green, B. (2002). Canny edge detection tutorial. Retrieved: March, 6, 2005.

[26]. Deb, D., Hariharan, S., Rao, U.M. and Ryu, C.H. (2008). Automatic detection and analysis of discontinuity geometry of rock mass from digital images. Computers & Geosciences. 34 (2): 115-126.

آنالیز اطلاعات ساختاری توده سنگ با استفاده از تکنیک‌های پردازش تصویر (مطالعه موردی: دیواره‌های شمالی معدن سنگ آهن چغارت)

محسن محبی*، علیرضا یاراحمدی بافقی، محمد فاتحی مرجی و جواد غلام نژاد

دانشکده مهندسی معدن و متالورژی، دانشگاه یزد، ایران

* نویسنده مسئول مکاتبات: mohebbi11@yahoo.com

چکیده:

وجود درزه و شکستگی در محیط‌های سنگی با تفکیک محیط به واحدهای کوچک‌تر به شدت بر رفتار توده سنگ تأثیرگذار اسـت. ایـن سـاختارها ضـمن توسـعه حرکات لغزشی و چرخشی، پتانسیل ناپایداری را تشدید می‌کنند. از این رو فرض ناپیوستگی، شرایط تحلیل را به صورت کامل نسـبت بـه تحلیـل پیوسـته متمـایز می‌کند. در تحلیل توده‌های سنگی، کسب اطلاعات هندسی و ساختاری ناپیوستگی‌ها در کنار خـواص مکـانیکی آن‌هـا بسـیار حـائز اهمیـت اسـت. جهـت‌گیـری، فاصله‌داری، گسترش و سایر ویژگی‌های هندسی سیستم‌های درزه‌ای توده سنگ و وضعیت نسبی آن با هندسه پروژه‌های عمرانی مـورد مطالعـه، الگـوی ریـزش و پتانسیل ریزش را تحت اثر قرار می‌دهد. از این رو در اولین مرحله در تحلیل توده سنگ، برداشت اطلاعات هندسی درزه اجتناب‌ناپـذیر اسـت و بـه عنـوان یکـی از مراحل بسیار مهم قبل از تحلیل قلمداد می‌شود. در این پژوهش ضمن معرفی روش‌های سنتی برداشت اطلاعات ساختاری ناپیوسـتگی‌هـا و معایـب موجـود، روش برداشت مبتنی بر آنالیز تصویر دیجیتال توسعه و در مطالعه موردی در رابطه با برخی از دیواره‌های سنگی موجود در معدن سنگ آهن چغارت به کـار گرفتـه شـده است. نتایج نشان می‌دهد که این روش، علاوه بر دقت بسیار مناسب در سنجش ریزترین ساختارهای موجود، سرعت برداشت را بهبود می‌بخشد و بنابرایـن مـی‌توانـد به عنوان تکنیکی نوین مورد استفاده قرار گیرد.

کلمات کلیدی: درزه نگاری، آنالیز تصویر دیجیتال، معدن سنگ آهن چغارت.